Pergamon

Int. J. Heat Mass Transfer. Vol. 39, No. 13, pp. 2811–2819, 1996

0017-9310/96 $15.00 + 0.00

0017-9310(95)00340-1

Monte Carlo simulation of radiative heat transfer in arrays of fixed discrete surfaces using cell-to-cell photon transport

BRUCE. J. PALMER

Energy and Environmental Science Division, Pacific Northwest National Laboratory†, Richland, WA 99352, U.S.A.

M. KEVIN DROST‡

Energy Division, Pacific Northwest National Laboratory, Richland, WA 99352, U.S.A.

and

JAMES R. WELTY

Oregon State University, Corvallis, OR 97331, U.S.A.

(*Received* 5 *January* 1993 *and in final form* 28 *June* 1995)

Abstract—An accurate simulation of radiative heat transfer in arrays of fixed discrete surfaces is challenging because of the complicated geometries that can shade and block many surfaces. This paper presents an innovative Monte Carlo scheme using cell-to-cell photon transport developed to simulate monochromatic radiation impinging on an array of fixed discrete elements. Results of the study show that cell-to-cell photon transport is an efficient method of simulating radiation heat transfer in complicated geometries. Sample calculations demonstrate the dependence of radiation heat transfer in the array on the geometry of the array elements. Copyright © 1996 Elsevier Science Ltd.

1. INTRODUCTION

In a recent review article, Howell indicates that radiative heat transfer in a fixed array of surfaces, where the surfaces have a fixed orientation, is a significant problem that is not being widely addressed [1]. In most problems involving radiative heat transfer in participating media, optical properties such as extinction coefficient and anisotropic scattering are generally treated as being independent of incident angle. However, when the orientation of an absorbing array is fixed, the scattering phase function depends on the angle of incidence as well as the angle of reflection, increasing the complexity of the problem. The additional complexity arises from both the anisotropy of the phase function of the individual reflector elements and the fixed geometrical relationship between different reflectors. Howell observes that methods for treating this situation are not available. This article presents an approach that models the absorbing array as discrete surfaces and uses a Monte Carlo algorithm to evaluate the radiation heat transfer in the array. The Monte Carlo approach was optimized for the general problem of two-dimensional (2D) arrays and can simulate a variety of arrays with different geometries, element cross-sections, and surface properties.

Monte Carlo modeling has been widely applied to radiative heat transfer, and the method is well documented [1–3]. In Monte Carlo simulations of radiative heat transfer problems, the energy emitted from a surface is simulated by a large number of photons. The photons are followed as they proceed from one interaction to another, with the results of each event being recorded. This continues until a photon either leaves the array or is absorbed. A sufficiently large number of photon trajectories must be simulated to ensure that variations in the results caused by random events are small. The results can be used to determine the fraction of emitted energy that has been absorbed on each surface and the fraction that has left the array.

The major challenges in a Monte Carlo model involve calculating photon trajectories and surface interactions. Determination of photon trajectories is particularly important because this calculation typically consumes up to 80% of the computer time used in a simulation [3]. Methods for modeling the interactions of a photon with a surface are described by several authors [2–6].

Most previous Monte Carlo models determine the location of a photon–surface interaction by finding

† Pacific Northwest National Laboratory is operated for the U.S. Department of Energy by Battelle Memorial Institute under Contract DE-AC06-76RLO 1830.

‡ Author to whom correspondence should be addressed.

NOMENCLATURE

L_w	array width
L_h	array height
$\mathbf{x}(\tau)$	parameterized straight line
$\mathbf{r}$	position vector
$\mathbf{s}$	photon direction vector
e_p	relative photon energy
$\hat{\mathbf{n}}$	surface unit normal vector
$\hat{\mathbf{z}}$	z axis normal vector
$\hat{\mathbf{e}}_n$	orthonormal basis vector normal to surface
$\hat{\mathbf{e}}_z$	orthonormal basis vector tangent to surface and parallel to z-axis
$\hat{\mathbf{e}}_\perp$	orthonormal basis vector tangent to surface and perpendicular to z-axis
$P_x(x)$	probability distribution function of photons coming out of array as a function of horizontal position.

Greek symbols

α	absorptivity
Δ_{src}	distance of source plane from front of the array
Δ_{det}	distance of detector plane from back of the array
θ	angle from surface normal (polar angle)
ρ_S	specularity
ρ'_S	relative specularity
ρ_D	diffuse relativity
ρ'_D	relative diffuse reflectivity
τ	parametric variable for straight line
ϕ	angle in surface plane (azimuthal angle)
φ	incident angle of photons going into the array.

the intercept of the vector describing the path of the photon and the lines describing each solid surface. The intercept closest to the initial location of the photon will be the location of the next surface–photon interaction [7]. The conventional scheme requires that all surfaces involved in the problem be checked for a possible intercept. When the problem includes a large number of surfaces, computing the location of a photon–surface interaction can become time-consuming.

For large numbers of surfaces, it becomes convenient to partition space into domains containing only a small number of surfaces. A photon entering a domain will check only the surfaces inside the domain for intersections. This is the basis for the Margolies shading algorithm described by Maltby and Burns [3], as well as the cell-to-cell transport algorithm described here. The cell-to-cell transport scheme simplifies identification of photon–surface interactions by dividing the array into rectangular regions that contain at most one reflecting element. Only the surfaces of the reflecting element within the cell need to be checked for possible intersections. For large arrays in which most of the photons travel only a short distance before encountering a surface, the cell-to-cell algorithm can dramatically reduce the number of comparisons required to find the next intersection of a photon with a surface.

2. CELL-TO-CELL PHOTON TRANSPORT

The cell-to-cell photon transport algorithm involves dividing the array into cells in which each cell contains a single array element. A photon is initially emitted into an exterior cell located on the boundary of the array and interacts with the element in that cell, resulting in the photon being absorbed, reflected out of the array, or transmitted to an adjacent cell. The procedure is repeated, tracking the photon as it moves from cell to cell until the photon is absorbed or exits the array. This scheme improves computational efficiency by limiting the number of surfaces that must be considered as possible candidates for the next photon–surface interaction. Cell-to-cell photon transport was originally reported by Drost [8].

The cell-to-cell algorithm subdivides the array into a set of parallel zones, each of which has the same width as the array, L_w, and then divides each zone into rectangular cells. Each cell has the same height as the zone, but the cell width is arbitrary. The only constraint is that the sum of all cell widths within a zone is equal to the zone width. A typical array of reflector elements is illustrated in Fig. 1(a), and the corresponding zones and cells are shown in Fig. 1(b). The array is assumed to be enclosed in a rectangular boundary located in the xy-plane. The faces of the array through which photons enter and exit are oriented parallel to the x-axis. The zones are also oriented parallel to the x-axis. The y-axis points into the array. The face of the array through which photons enter is located at $y = 0$, and the left-boundary of the array is fixed along the line $x = 0$. The right-hand boundary is located at $x = L_w$. The sum of all the zone heights is equal to the height of the array, L_h, and photons exit the array by crossing the line at $y = L_h$.

The boundaries of the array at $x = 0$ and $x = L_w$ can be treated as either regular surfaces or as periodic boundaries. If the boundaries are treated as regular surfaces, photons encountering them can be absorbed, specularly reflected, or diffusely reflected. If the boundaries are periodic, a photon that exists one side of the array enters the array from the other side traveling in the same direction and with the same (y, z) coordinate.

Cell-to-cell photon transport modeling requires two

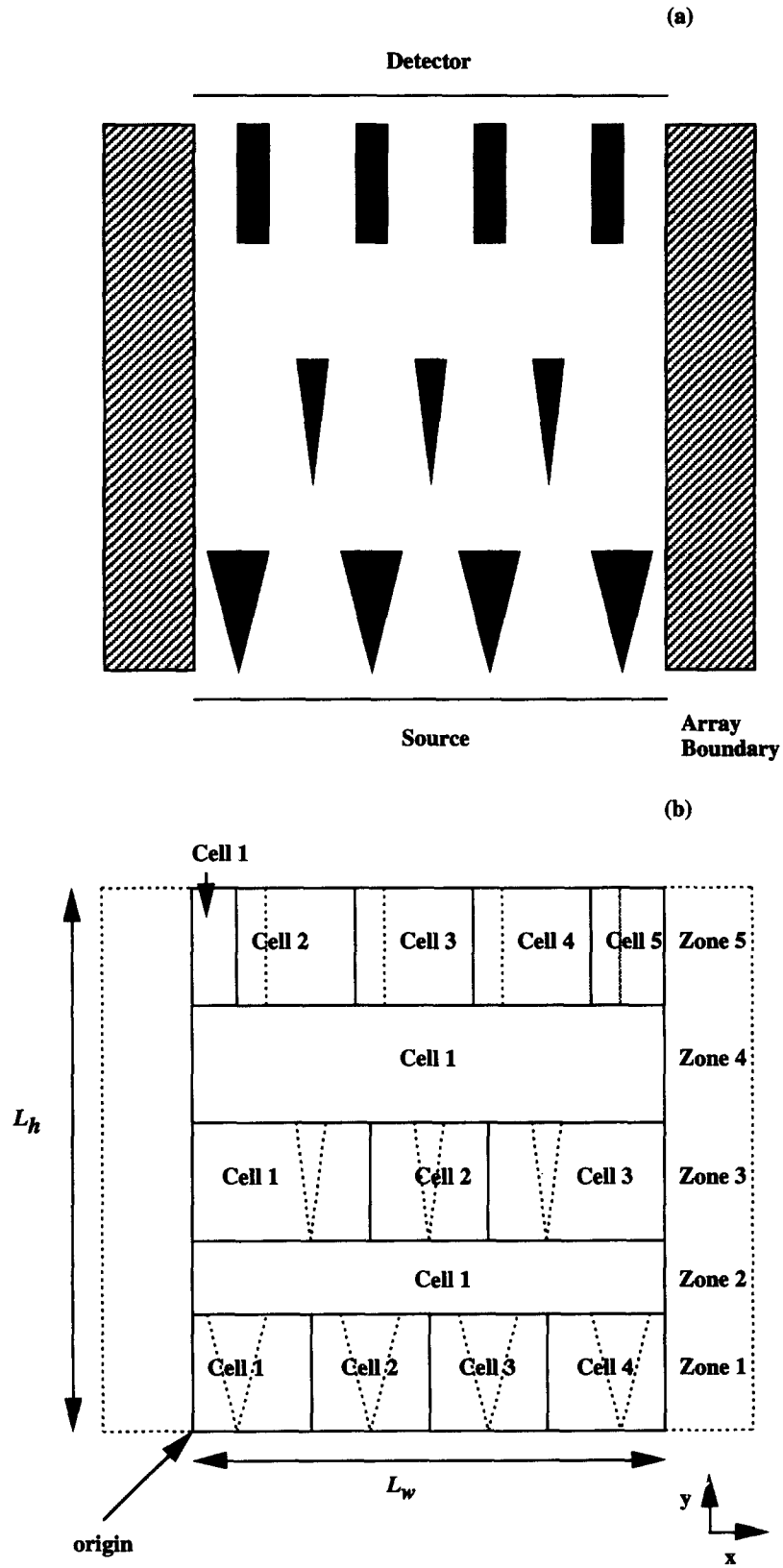

Fig. 1. (a) Schematic of an array containing both rectangular and wedge-shaped elements. (b) Zone and cell boundaries for the array shown in (a).

sets of calculations. The first set determines the movement of a photon from one cell to another; the second determines the outcome of a photon–cell interaction. A photon trajectory is started by emitting a photon into a cell with a face located on the illuminated side of the array. The illuminated sides lie along the x-axis. The photon is initially located on the cell boundary with a known position and direction. When the calculation of the photon trajectory within the cell is completed, the photon is again located on the boundary of the cell with a known position and exit direction.

If the photon crosses a vertical cell boundary, then the direction and location of the photon as it enters the adjacent cell is easily determined. If the photon crosses a zone boundary, it is necessary to identify the cell that the photon enters by comparing the x-coordinate of the photon with the cell boundary locations in the next zone. Each time a photon exits a cell through one of the vertical cell boundaries, it is also necessary to check for an interaction between the photon and an array boundary. Similarly, when a photon enters a new zone, the zone number is checked to determine if the photon has exited the array. Once the next cell is determined, the procedure is repeated until the photon is absorbed or exits the array. The cell-to-cell algorithm decomposes the trajectory of the photon through the array into a sequence of short trajectories, each taking place in a single cell. The trajectories are matched up at the cell boundaries so that the path of the photon through the lattice corresponds to the path that would be obtained using more conventional means.

The cell-to-cell tracking scheme is independent of the reflector element geometries contained within each cell. Individual cell models can be changed and new models developed without affecting the cell-to-cell tracking scheme. Each cell model receives information on the photon's location and incoming angle from the cell-to-cell tracking algorithm and returns the new location and exit direction of the photon. In essence, the trajectory of the photon through the array is broken up into a sequence of subtrajectories with each subtrajectory being contained entirely within a single cell.

Most of the calculations required to evaluate the trajectory of a photon inside a cell consist of finding the intersections of various straight lines. The photon trajectory, as well as the surface elements inside the cell and the cell boundary itself, are all straight-line segments. For these calculations, the most convenient form for describing a line is to use a parameterized vector equation. The straight line $\mathbf{x}(\tau)$ is given by the formula

$$\mathbf{x}(\tau) = \mathbf{r} + \tau\mathbf{s}. \tag{1}$$

This formula is applicable to both 2D and 3D systems; however for 2D problems, only the projection of equation (1) into the xy-plane is needed. Different values of τ correspond to different points along the line $\mathbf{x}(\tau)$. It is sometimes useful to think of $\mathbf{x}(\tau)$ as the motion of a particle traveling at constant velocity $\mathbf{s}$. When $\tau = 0$, the particle is located at $\mathbf{r}$. The intersection of two arbitrary lines, $\mathbf{x}(\tau)$ and $\mathbf{x}'(\tau')$, can be found using formulas from elementary linear algebra. The intersection of $\mathbf{x}(\tau)$ and $\mathbf{x}'(\tau')$ is equivalent to the condition.

$$\mathbf{r} + \tau\mathbf{s} = \mathbf{r} + \tau'\mathbf{s}'. \tag{2}$$

Equation (2) is easily solved for τ and τ' to get

$$\tau = \frac{1}{s'_x s_y - s_x s'_y}[s'_y(r_x - r'_x) - s'_x(r_y - r'_y)]$$

$$\tau' = \frac{1}{s'_x s_y - s_x s'_y}[s_y(r_x - r'_x) - s_x(r_y - r'_y)].$$

These calculations do not require any special functions (such as square roots or trigonometric functions) so they are performed quickly on most computers.

For simulations on arrays containing reflector elements with circular cross-sections, it is also necessary to calculate the intersection of a line with a circle. The equation for a circle of radius a centered at $\mathbf{c}$ is

$$|\mathbf{x} - \mathbf{c}|^2 = a^2.$$

Substituting the line $\mathbf{x}(\tau)$ for $\mathbf{x}$ in this equation and solving for τ gives

$$\tau = -\mathbf{s}\cdot(\mathbf{r} - \mathbf{c}) - \sqrt{([\mathbf{s}\cdot(\mathbf{r} - \mathbf{c})]^2 - |\mathbf{r} - \mathbf{c}|^2 + a^2)}.$$

This root corresponds to the point of closest contact. The calculation of τ can be broken up into several steps to avoid unnecessary calculation of the square root.

When compared to other photon transport schemes, the conditional branching approach used in the cell-to-cell transport scheme will generally reduce numerical operations because cell geometries are arranged to ensure that the photon will interact with only one solid surface. After that interaction, the photon exits the cell. On scalar computers, this approach gives very good results. The calculations reported here took between 3 and 10 h for 2×10^6 separate photon trajectories on a SPARC II workstation. Because both the cell-to-cell transport scheme and the photon dynamics within the cell use highly branched conditional structures, the code was not significantly improved by going to a vector machine such as a Cray II. However, because the individual trajectories do not interact with each other, Monte Carlo modeling is easily adapted to parallel architecture machines. Each processor can run independent simulations, and the results are collected at the end of the simulation.

The only remaining consideration is to calculate the post-collision direction for photons that hit one of the elements in the array (or the boundaries of the array if periodic boundary conditions are not used). This depends on the optical properties of the surfaces. For the calculations reported here, the photon can be absorbed with probability α (absorptivity), specularly

reflected with probability ρ_S (specular reflectivity), or diffusely reflected with probability ρ_D (diffuse reflectivity). In the most general case, these quantities are functions of the polar and azimuthal angles of the incoming photon but, in these calculations, they are assumed to be constant. The absorptivity, specular reflectivity, and diffuse reflectivity satisfy the relation,

$$\alpha+\rho_S+\rho_D = 1.$$

The current version of the computer code assumes that all surfaces within a cell have the same values of α, ρ_S and ρ_D but different cells can have different values for these parameters. The array boundaries' optical properties can be independently specified if periodic boundary conditions are not imposed.

Photon absorption is computed by initially assigning a unit "energy", e_p, to each photon trajectory. Each time the photon collides with a surface with nonzero α, the post-collision energy, e'_p is calculated according to

$$e'_p = (1-\alpha)e_p.$$

The fractional energy absorbed, αe_p, can be assigned to the cell or zone for subsequent statistical analysis. If the photon energy falls below some preset minimum value, e_{min}, the trajectory is terminated.

Most collisions with a reflector surface result in either a specular or a diffuse reflection. The relative probabilities for specular and diffuse reflections, ρ'_S and ρ'_D, are

$$\rho'_S = \frac{\rho_S}{\rho_S+\rho_D}$$

$$\rho'_D = \frac{\rho_D}{\rho_S+\rho_D}.$$

The surface properties can be specified using either α, ρ_S, ρ_D or α, ρ'_S, ρ'_D.

When the photon trajectory intersects a surface, a random number, $x \in [0, 1]$, is generated to determine whether the reflection is specular or diffuse. If $x < \rho'_S$, the reflectance is specular; otherwise, it is diffuse. If the reflection is specular, the postcollision direction, $\mathbf{s}'$, is given by the formula

$$\mathbf{s}' = \mathbf{s}-2(\mathbf{s}\cdot\hat{\mathbf{n}})\hat{\mathbf{n}}. \tag{3}$$

where $\mathbf{s}$ is the precollision photon direction and $\hat{\mathbf{n}}$ is an outwardly directed normal vector to the surface at the point of collision.

For diffuse reflections, the angle that the incoming photon makes with the surface normal is denoted by θ, while the angle the outgoing photon makes with the normal is denoted by θ'. The azimuthal angle of the outgoing photon, ϕ', is the angle formed between the projections in the plane containing the surface of the incoming and outgoing photon directions. The coordinates for surface scattering are illustrated schematically in Fig. 2. The probability distributions for the angles θ' and ϕ' of the outgoing photon relative

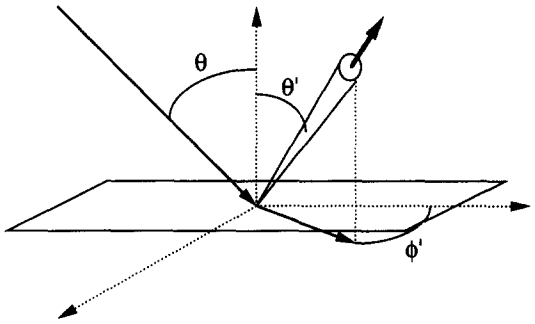

Fig. 2. Definition of angles for diffuse reflections.

to the surface normal and some axis in the tangent plane of the surface are, respectively.

$$P(\theta')\,d\theta' \sim \cos\theta'\,d\cos\theta'$$

$$P(\phi') \sim d\phi'.$$

For random numbers $x,y \in [0, 1]$, θ' and ϕ' are given by

$$\theta' = \cos^{-1}(\sqrt{x})$$

$$\phi' = 2\pi y.$$

Because the arrays are uniform in the $\hat{\mathbf{z}}$ direction, an orthonormal basis, $\hat{\mathbf{e}}_n$, $\hat{\mathbf{e}}_z$, $\hat{\mathbf{e}}_\parallel$, can be constructed at the collision point using the relations

$$\hat{\mathbf{e}}_n = \hat{\mathbf{n}}$$

$$\hat{\mathbf{e}}_z = \hat{\mathbf{z}}$$

$$\hat{\mathbf{e}}_\parallel = \hat{\mathbf{n}}\times\hat{\mathbf{z}}. \tag{4}$$

The outgoing photon direction is then

$$\mathbf{s}' = \cos\phi'\sin\theta'\hat{\mathbf{e}}_z+\sin\phi'\sin\theta'\hat{\mathbf{e}}_\parallel+\cos\theta'\hat{\mathbf{e}}_n. \tag{5}$$

Using equations (4), the vector $\hat{\mathbf{e}}_n$, $\hat{\mathbf{e}}_z$ and $\hat{\mathbf{e}}_\parallel$ can be written in the global (x, y, z) coordinates used to describe the array. The vector $\mathbf{s}'$ can then be calculated in the global coordinates using equation (5).

The array pictured in Fig. 1(a) also includes the photon source and detection plane. Photons originate in a plane parallel to the xz-plane and set a distance Δ_{src} from the front of the array. Depending on the type of illumination, photons can be distributed in the source plane in a variety of ways. The calculations reported here use a collimated beam as the photon source. The beam is assumed to have a Gaussian profile normal to the beam axis. All photons have the same initial direction, $\mathbf{s}$, but the spatial distribution of photons in the source plane is a Gaussian centered at a value of $x = x_0$, $z = 0$. If the beam is oriented an angle φ from the y axis, the Gaussian is broadened by a factor of $1/\cos\varphi$ in the x-direction. Photons are detected when they cross a plane parallel to the xz plane and set a distance Δ_{det} behind the array.

The Monte Carlo algorithm described above was

the basis for the MCLITE† computer code. The MCLITE code was validated by comparing the results of MCLITE with an earlier cell-to-cell transport code, VORRUM†. The results were identical within statistical uncertainties for a range of array geometries and surface properties. VORRUM validation is described by Drost *et al.* [8, 9]. The current version of MCLITE supports modeling of reflector elements with triangular, cylindrical and rectangular cross-sections.

3. RESULTS

To illustrate the capabilities of the MCLITE computer code, simulations on three large arrays were performed. The arrays were chosen to study whether or not the global properties of the array eventually become independent of the detailed structure of the array for large arrays. The arrays were composed of reflector elements with cylindrical and triangular cross-sections. The triangular and cylindrical reflector elements both presented the same cross-section at normal incidence, and the geometrical arrangement of the elements was the same for all three arrays.

The reflector elements in each array were centered at the vertices of a triangular lattice. The first array was composed of only triangular reflector elements; the second array was composed of only cylindrical reflector elements; and the third array was a random 50 : 50 mixture of cylindrical and triangular elements. The triangular array elements were isosceles triangles with a base of width of 1 unit and a height of 1 unit. The triangles were oriented so that the base was parallel to the x-axis and the apex was pointed in the negative y-direction. The cylinders were 1 unit in diameter. Each array was composed of 30 rows and each row contained 59 reflector elements. Each row was 1 unit in height, and the center-to-center distance between array elements in each row was 2 units. The array elements in successive rows were offset from each other by 1 unit, and each row was separated from the next by a gap of 0.732 units. A small section of the mixed array, along with the dimensions, is shown in Fig. 3. The overall dimensions of the arrays were 118 units in the x-direction and 51.229 units in the y-direction. Periodic boundary conditions were imposed on all arrays.

The array elements in all three arrays were given nonabsorbing surfaces. For one set of calculations, the surfaces were perfect specular scatterers; for the other, the surfaces were perfect diffuse scatterers. The arrays were illuminated by a collimated beam with a Gaussian profile in the plane normal to the beam axis. The half-width at half maximum of the Gaussian profile was 5.89 units. All the photons in the incident beam were traveling in the same direction with no spreading. The incident beam was parallel to the xy-plane and was deflected from the y-axis by an angle φ. The center of the beam was located 30 units along the x-axis. The source and detection planes were both set 0.001 units from the front and back of the array, respectively. Because periodic boundary conditions were used, the incident beam was replicated in each periodic unit of the array.

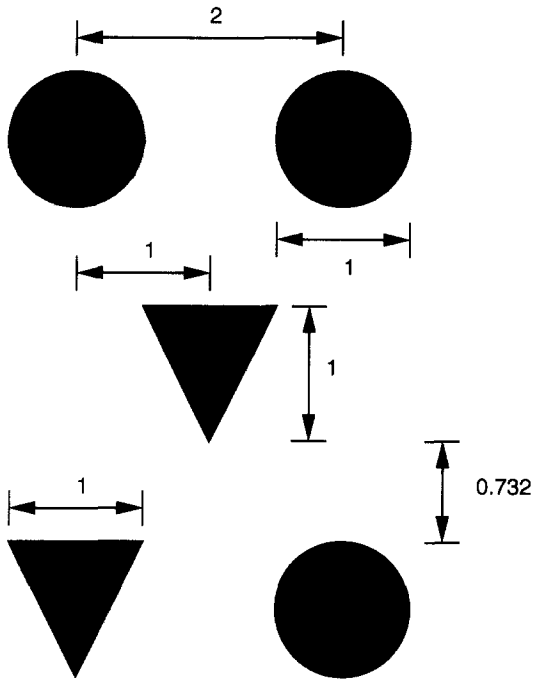

Fig. 3. Representative portion of mixed array with dimensions in arbitrary units.

Two sets of surface properties were used. For one set of calculations, all the reflector elements were given completely specular surfaces ($\rho_S = 1.0$) while, for the second set, the reflector elements were given completely diffuse surfaces ($\rho_S = 0.0$). The emissivity was zero in all cases so that there was no absorption by the array itself.

Two angles of incidence were investigated, $\varphi = 0°$ and $\varphi = 29°$. The choice of $\varphi = 29°$ corresponds to a beam that is pointed almost directly down the channels in the array, located at $\pm 30°$ from the y axis. The transmittance (T) and reflectivity (R) of the arrays for both specular and diffuse surface are listed in Table 1.

Not surprisingly, the specular arrays show more varied behavior than the diffuse arrays. For normal incidence, the reflectance of the specular arrays saturates, in the sense that all three arrays are highly reflective. The transmittance, however, is still sensitive to the details of the array elements and varies by more than a factor of two between the three different arrays. For $\varphi = 29°$, all three arrays show significant differences in behavior. The transmittance goes up in all cases but not consistently. The triangular array, which had the lowest transmittance at normal incidence, still

† Developed by researchers at Pacific Northwest Laboratory, Richland, WA.

Table 1. Transmittance and reflectance for incident angles of $\varphi = 0°$ and $\varphi = 29°$ for arrays with specular ($\rho_S = 1.0$) and diffuse ($\rho_S = 0.0$) surfaces

Array	ρ_S	φ	T	R
Triangular	1.0	0°	0.021	0.979
Cylindrical	1.0	0°	0.044	0.956
Mixed	1.0	0°	0.054	0.946
Triangular	1.0	29°	0.057	0.943
Cylindrical	1.0	29°	0.204	0.796
Mixed	1.0	29°	0.140	0.860
Triangular	0.0	0°	0.032	0.968
Cylindrical	0.0	0°	0.024	0.976
Mixed	0.0	0°	0.028	0.972
Triangular	0.0	29°	0.198	0.802
Cylindrical	0.0	29°	0.166	0.834
Mixed	0.0	29°	0.125	0.875

has the lowest transmittance at $\varphi = 29°$. The relative transmittance of the cylindrical and mixed arrays is now the reverse of the normal incidence case, with the cylindrical array having the higher transmittance. Furthermore, the transmittance of the cylindrical and mixed array is fairly high, while the transmittance of the triangular array remains low.

More striking differences between the three specular arrays can be seen by examining the spatial distribution of photons leaving the back of the array. The distribution of photons is given by $P_x(x)$, which is the probability of finding a photon at the back of the array ($y = L_h$) at position x. The distribution $P_x(x)$ is normalized so that the integral

$$\int_0^{L_w} P_x(x')\,dx'$$

equals the total transmittance. The function $P_x(x)$ can be interpreted as the relative intensity seen by a detector with a 2π solid acceptance angle centered at x. The function $P_x(x)$ is computed by dividing the interval $[0, L_w]$ into 59 bins, one for each array element in the last row, and binning the outgoing photons as a function of x. The distribution of the photon beam at the backplane of the array in the absence of any array elements is shown in Fig. 4 for both $\varphi = 0°$ and $\varphi = 29°$.

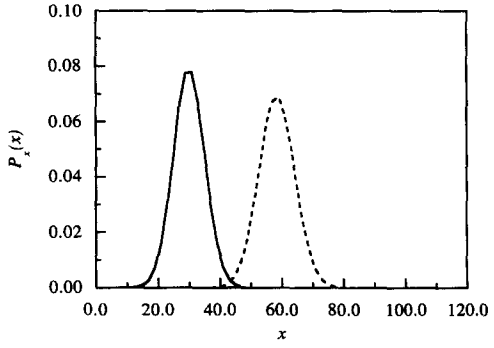

Fig. 4. Profiles $P_x(x)$ for unobstructed beam. Solid line is for $\varphi = 0°$; dotted line is for $\varphi = 29°$.

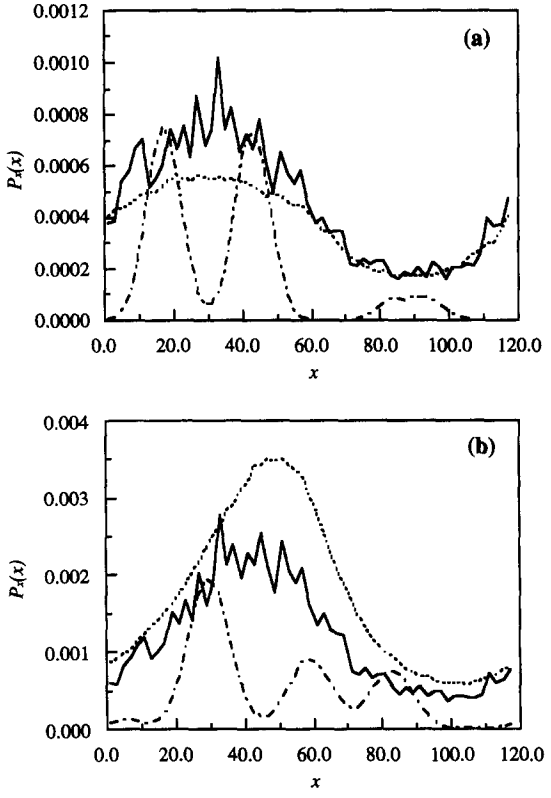

Fig. 5. (a) Profiles $P_x(x)$ for specular arrays with $\varphi = 0°$. Mixed array (——). Triangular array (—·—·—). Cylindrical array (....). (b) Profiles $P_x(x)$ for specular arrays with $\varphi = 29°$. Mixed array (——). Triangular array (—·—·—). Cylindrical array (....).

The $P_x(x)$ for the three specular arrays are shown in Fig. 5(a) for the case $\varphi = 0°$. The $P_x(x)$ for the cylindrical and mixed arrays are qualitatively similar, although the mixed array shows more sharp variations in intensity. The maximum uncertainty in $P_x(x)$ is not more than 2.5×10^{-5} for any of the curves presented here, so the variations in the mixed-array curve are real and not the result of noise in the statistics. These variations are characteristic of all the $P_x(x)$ for the mixed array.

The $P_x(x)$ for the triangular array is completely different from the curves obtained for the cylindrical and mixed arrays. Instead of showing the broad distribution with a maximum centered at $x = 30$, the distribution has two peaks at approximately $x = 20$ and $x = 40$, with a minimum at $x = 30$. There is also an additional side peak near $x = 90$.

The broadening of the incident beam for the cylindrical and mixed lattices can be rationalized by a diffusion model for the photon motion. For the triangular lattice, the idea that photons are diffusing obviously breaks down. Because of the small number of possible surface orientations, it might be argued that the photons sample a relatively small number of distinct paths through the lattice. The width of the individual peaks is comparable to the width of the

incident beam, supporting the notion that there are only a few paths through the lattice. However, the possibility that only a few paths are being taken through the lattice is surprising, because the sides of the triangles are oriented at 26.5651° from the vertical. This angle is not a rational fraction of π. After several collisions, the array should randomize photon directions, although possibly not as quickly as for the cylindrical and mixed lattice.

The distributions $P_x(x)$ for $\varphi = 29°$ are shown in Fig. 5(b). The cylindrical and mixed arrays again show a broad peak. For the cylindrical array, the peak is centered at about $x = 50$, while for the mixed array, the peak appears shifted slightly to $x = 40$–45. The unobstructed beam, however, is centered at $x = 60$. The beam orientation does affect the position of maximum intensity at the back of the array, but collisions with the reflector elements result in a smaller shift than that for the unobstructed beam. The intensity maximum for the cylindrical array is higher than for the mixed array, which correlates well with the behavior of the total transmittance. As in the normal incidence case, the behavior of $P_x(x)$ for the triangular array is completely different from that for the cylindrical and mixed arrays. The distribution has three distinct peaks, with the largest centered near $x = 30$. The discrete peaks, and the lack of broadening again suggest that the photons are taking only a few discrete paths through the array.

The fact that the peaks for the cylindrical and mixed lattice are shifted from $x = 30$ but are not centered at the unobstructed beam maximum can be explained also by a diffusion picture of photon motion. For an incident angle of 29°, a significant fraction of photons is able to travel deep into the array before hitting one of the reflector elements. After the first collision, the motion of the photons is diffusive. The center of the peak in $P_x(x)$ should therefore correspond to the center of the distribution of first collisions.

For diffuse reflector surfaces, it would be expected that the reflectance and transmittance would show less variability between the different arrays than for the specular surfaces. These expectations are partially borne out by the results in Table 1. For normal incidence, all three arrays are again highly reflective. The transmittances, although small, are relatively close to each other compared to results for the specular case. Interestingly, the transmittance for the triangular array is now the highest for the three arrays instead of the lowest. For $\varphi = 29°$, the transmittance increases significantly for the three arrays. The triangular reflector elements again give the highest transmittance, but the spread in transmittance values is smaller than for the specular case.

The behavior of the distributions $P_x(x)$ parallels the transmittance for the diffuse arrays. The $P_x(x)$ for $\varphi = 0°$ are shown in Fig. 6(a) for the three arrays. The three curves show a broad maximum centered at $x = 30$, with the relative intensities ordered in the same way as the total transmittances. The $P_x(x)$ for

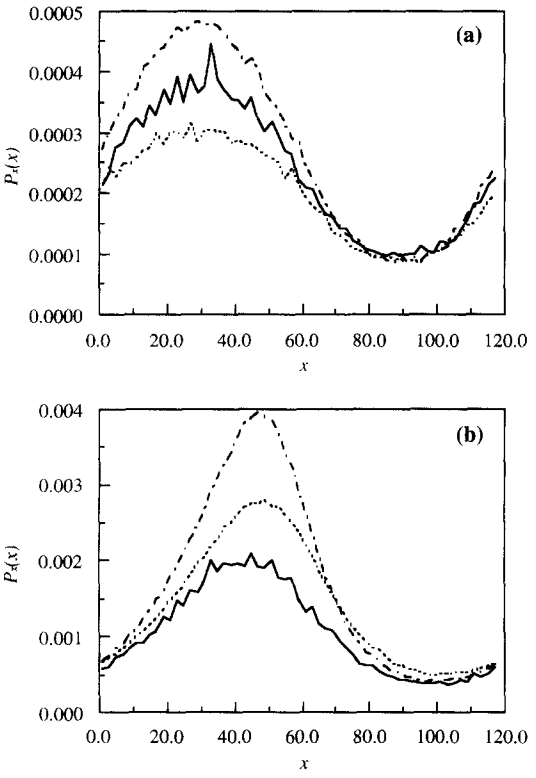

Fig. 6. (a) Profiles $P_x(x)$ for diffuse arrays with $\varphi = 0°$. Mixed array (——). Triangular array (— · — · —). Cylindrical array (. . . .). (b) Profiles $P_x(x)$ for diffuse arrays with $\varphi = 29°$. Mixed array (——). Triangular array (— · — · —). Cylindrical array (. . . .).

$\varphi = 29°$ are shown in Fig. 6(b). The three curves show a broad maximum near $x \sim 50$. Again, the ordering of the relative intensities in $P_x(x)$ matches the ordering of the total transmittance for each of the arrays. Both the broadening of the intensity maximum and the shifting of the peak for the $\varphi = 29°$ case are consistent with the diffusion picture of photon motion in these arrays.

4. CONCLUSIONS

The cell-to-cell transport algorithm can efficiently model radiative heat transfer in arrays composed of fixed discrete surfaces. The method allows rapid computation of photon paths through the array and is flexible enough to permit examination of a wide variety of geometrical arrangements. Furthermore, the algorithm can be extended to handle other element cross-section shapes in addition to the triangular and cylindrical elements described in this study. The algorithm can also be extended to 3D geometries. The cell-to-cell algorithm is applicable to any problem requiring calculation of photon paths; it can also be used to model radiative exchange and the calculation of view factors [10].

The calculations performed in this paper provide a good indication of the efficiency of the cell-to-cell

transport algorithm. The mixed array contains approximately 2500 surfaces for the triangular-array elements and another 800 or so surfaces for the cylindrical elements, which are arranged in a nonsymmetric pattern. Using the cell-to-cell transport algorithm, 2×10^6 trajectories could be run in 3–10 h on a standard workstation. (The $\varphi = 0°$ calculations were near the 3-h end of this range; the $\varphi = 29°$ calculations were closer to 10 h.)

The calculations in this paper also indicate that the global optical properties of regular arrays retain a sensitive dependence on the detailed structure of the array, even in the large array limit. For the cylindrical array, where the motion of photons should be highly randomized after the first one or two collisions, there are still quantitative differences between the arrays with specular and diffused reflector elements. The triangular array behaves differently, both quantitatively and qualitatively, from the cylindrical and mixed arrays for the specular case and shows large quantitative differences in the diffuse case. Furthermore, there does not appear to be any consistent pattern of behavior for the array transmittance and reflectance as a function of incident angle or surface properties. Based on the results presented here, it would be difficult to predict *a priori* which array would have the highest reflectance and transmittance for a given set of surface properties.

Acknowledgements—The research reported in this paper was funded by the U.S. Department of Energy's Basic Energy Sciences Program. We would like to thank Dr Oscar Manley of the Basic Energy Sciences Program for his support and guidance.

REFERENCES

1. J. R. Howell, Thermal radiation in participating media: the past, the present, and some future possibilities, *J. Heat Transfer* **110,** 1220–1230 (1988).
2. R. Siegel and J. R. Howell, *Thermal Radiation Heat Transfer*. McGraw-Hill, New York (1972).
3. J. D. Maltby and P. J. Burns, Performance, accuracy and convergence in a three-dimensional Monte Carlo radiative heat transfer simulation, *Numer. Heat Transfer* **19,** 191–209 (1991).
4. R. S. Yang, Heat transfer throughout a randomly packed bed of spheres by the Monte Carlo method, Ph.D. Thesis, University of Texas, Austin, TX (1981).
5. A. Haji-Sheikh, Monte Carlo methods. In *Handbook of Numerical Heat Transfer*, pp. 673–722. Wiley Interscience, New York (1988).
6. P. J. Burns and D. V. Pryor, Vector and parallel Monte Carlo radiative heat transfer simulation, *Numer. Heat Transfer* **16,** 97–124 (1989).
7. R. C. Corlett, Direct Monte Carlo calculation of radiative heat transfer in vacuum, *J. Heat Transfer* **88,** 376–382 (1966).
8. M. K. Drost, Volumetric receiver development—a heat transfer and design evaluation of an advanced air heating solar thermal central receiver concept, Ph.D. Thesis, Oregon State University, Corvallis, OR (1985).
9. M. K. Drost and J. R. Welty, Monte Carlo simulation of radiative heat transfer in arrays of fixed discrete surfaces using cell-to-cell photon transport. In *Developments in Radiative Heat Transfer*, pp. 85–92. American Society of Mechanical Engineers, New York (1992).
10. M. K. Drost and J. R. Welty, Volumetric receiver radiation heat transfer. In *Heat Transfer*, Denver A.I.Ch.E. Symposium Series, Vol. 81, No. 245, pp. 220–226. American Institute of Chemical Engineers, New York (1985).